A Gradient-Descent Optimization Assisted Gray-Box Impedance Modeling of EV chargers

Wang, Lu; Qin, Zian; Bauer, Pavol

DOI
10.1109/TPEL.2023.3267151

Publication date
2023

Document Version
Final published version

Published in
IEEE Transactions on Power Electronics

A Gradient-Descent Optimization Assisted Gray-Box Impedance Modeling of EV Chargers

Lu Wang, *Student Member, IEEE*, Zian Qin, *Senior Member, IEEE*, and Pavol Bauer, *Senior Member, IEEE*

***Abstract*—Extracting an electric vehicle (EV) charger's input impedance with the analytical model (white-box approach) or the frequency sweep (black-box approach) is limited by the parameter confidentiality or the measurement noise, respectively. To overcome these challenges, a gradient-descent (GD) optimization-based gray-box modeling approach is proposed. To start with, a sensitivity study on the analytical impedance model of an EV charger with a typical controller is carried out to identify the influential frequency range per controller and circuit parameter. On top of that, given an EV charger with unknown control and circuit information, a GD optimization-based algorithm for multiple parameter estimation is designed to identify the unknown controller and circuit parameters based on the measured impedance, by assuming the EV charger is using the typical controller. Then, an analytical input impedance of the black-box EV charger can be obtained. Moreover, the low-accuracy issue commonly encountered when estimating multiple parameters with GD optimization is mitigated with the proposed algorithm. Compared to pure frequency sweep, the proposed approach achieves a higher accuracy for the coupling impedance and a comparable accuracy for the diagonal impedance. The effectiveness of the proposed approach is validated by experimental results.**

***Index Terms*—Gradient-descent (GD) optimization, impedance modeling, parameter estimation.**

I. Introduction

With the electrification process of transportation systems, massive installations of high-power-electric-vehicle chargers (HPEVCs) are approaching. As grid-connected power-electronic converters (PECs), the impacts of HPEVCs on the harmonic compatibility and the stability of power grids are inevitable [1]. Such impacts of PECs have caused issues in electric vehicle (EV) charging stations [2], [3], as well as other PEC-based systems, e.g., photovoltaic farms and wind farms [4], [5].

The impedance-based approach is promising in analyzing the stability [6], [7], [8], and harmonic emission [9] of PEC-based systems, e.g., EV charging stations. Extracting the input impedance of an HPEVC is indispensable to apply this approach. The input impedance can be obtained with the analytical impedance model, which is known as the white-box approach. However, a charger's analytical impedance model is not always provided by every vendor. Alternatively, the user of the charger, i.e., a charging station operator, can establish their own analytical model using the approaches in [10], [11], and [12]. However, the charger's design details are required, which are confidential and concealed by the manufacturers. Here, the design details include the circuit topology, control strategy, and the parameters of the passive components and the tuned controllers. Compared to the unknown circuit topology and control strategy, which are less problematic because industrial companies follow some mainstream designs, the unknown controller and circuit parameters can vary a lot from one charger to another. Thus, extracting the input impedance with the white-box approach might be difficult in practice.

One may argue that the impedance measured with a black-box approach, namely frequency sweep, can be used instead for the stability analysis and the harmonic emission evaluation. However, the measured impedance can have significant errors [12], [13]. Furthermore, HPEVCs' input impedance is also dependent on their charging power. Therefore, measuring the chargers' input impedance at all power and frequencies of interest to obtain adequate impedance information is too time consuming.

To overcome the challenges encountered with the white-box and black-box modeling approaches, the gray-box modeling approaches [14] can be used. A gray-box impedance model has the same structure as the white-box impedance model, which is derived through the physics regulating an HPEVC. The unknown parameters needed to analytically extract the input impedance can be estimated by updating the unknown parameters iteratively to minimize the mean square error (MSE), i.e., the average squared difference between the estimated impedance and the measured impedance. Therefore, the multiple-parameter estimation problem is an optimization problem. Such a problem can be solved by gradient-descent (GD) optimization, which is widely used in parameter estimation problems [15], [16], [17], [18], [19]. The aforementioned approaches are compared in Table I to clarify the advantages of gray-box modeling approaches.

However, one issue can arise in the parameter estimation, which leads to the low accuracy of the obtained gray-box model. Since the aforementioned parameter estimation approach generally results in a nonconvex optimization problem [16], the evaluated multiple parameters can converge to wrong values, which do not minimize the MSE. Thus, the estimation results

Manuscript received 25 August 2022; revised 22 January 2023 and 7 March 2023; accepted 3 April 2023. Date of publication 17 April 2023; date of current version 19 May 2023. This project has received funding from the Electronic Components and Systems for European Leadership Joint Undertaking under grant agreement No 876868. This Joint Undertaking receives support from the European Union's Horizon 2020 research and innovation programme and Germany, Slovakia, Netherlands, Spain, Italy. Recommended for publication by Associate Editor A. Barrado. *(Corresponding author: Zian Qin.)*

The authors are with the Department of Electrical Sustainable Energy, DC Systems, Energy Conversion and Storage Group, Delft University of Technology, 2628, CD Delft, The Netherlands (e-mail: l.wang-11@tudelft.nl; z.qin-2@tudelft.nl; p.bauer@tudelft.nl).

Color versions of one or more figures in this article are available at https://doi.org/10.1109/TPEL.2023.3267151.

Digital Object Identifier 10.1109/TPEL.2023.3267151

TABLE I
COMPARISON OF DIFFERENT APPROACHES OBTAINING A CHARGER'S INPUT IMPEDANCE

	Analytical model	Measured model	Normal GD optimization based gray-box model	Proposed gray-box model
How does it look like?	$Z_o = f_k(x_1, x_2, ..., x_n)$ f_k is shaped by different control of the charger, x_i include both control and hardware parameters.	$Z_o = \Delta v(f)/\Delta i(f)$ $\Delta v(f)$ and $\Delta i(f)$ are small perturbations for impedance measurement.	$\hat{Z}_o = f_k(\hat{x}_1, \hat{x}_2, ..., \hat{x}_n)$ $\hat{x}_i$ are estimated parameters of the charger by using GD optimization based on measured data.	
Need to know the control strategy f_k of the charger?	Yes, but usually there are only a few typical variations of f_k in EV charger,which can easily be covered.	N.A.	Yes, but usually there are only a few typical variations of f_k in EV charger,which can easily be covered.	
Need to know the parameters $\hat{x}_i$ of the charger?	Yes, and the parameters are usually difficult to obtain, especially the control parameters.	N.A.	No, the parameters x_i of the charger are estimated.	
Is sensitive to measured noise?	N.A.	Yes	A little, by GD optimization, the impact of the measured noise is minimized.	
Can have significant errors when the measured perturbation is small? (i.e., ¡ 0.1 A)	N.A.	Yes	No, the immeasurable points can be eliminated, since this is essentially an analytical model. Only sparse measurements are needed to identify $\hat{x}_i$.	
Requiring of large amount of measurement data to reflect the charger's impedance in different operation conditions?	No	Yes	No, only small amount of measurement data is needed to identify $\hat{x}_i$.	
Others	N.A.		The chance that the GD optimization converges wrongly increases exponentially as the number of $\hat{x}_i$ increases, which leads to wrong estimation. GD optimization is more effective when the number of $\hat{x}_i$ is small.	By analyzing the influential frequency range of different $\hat{x}_i$, it is found that in some frequency ranges, $\hat{Z}_o$ is only shaped by one or several $\hat{x}_i$. On top of that, the sequence of $\hat{x}_i$ for identification is defined. As a result, the GD optimization can converge correctly, even there are several $\hat{x}_i$ coupled together.

are inaccurate. Such an issue has been reported in [17], where the power transformer parameters need to be estimated. The issue can be solved by adding constraints determined by the physics in an application. For instance, in [18], the initial parameter estimates and constraints for power transformers are studied to help the estimated transformer parameters converge correctly to improve the accuracy of the gray-box model. However, the study on how to solve the wrong convergence issue when estimating an HPEVC's parameters with their input impedance is not found in the literature. A similar concept is found in [20], where a gray-box impedance modeling approach for wind turbine inverters is proposed. However, the details on how to solve the wrong convergence issue are overlooked. Overall, the issue stems from the parameters' scaling difference and the influence of saddle points [21].

This article proposes a gray-box modeling approach for HPEVC. The low estimation accuracy issue is addressed by a proposed estimation approach. We start with deriving the mathematical expressions of the elements in the input impedance matrix of a typical HPEVC. On top of that, a sensitivity study is carried out to clarify how the input impedance is influenced by the parameters, namely the inductance of the power filter, the capacitance of the dc-link capacitor, and the controller parameters. It is found that the impedance is sensitive to the variation of different parameters in different frequency ranges. Besides, each element in the input impedance matrix is only influenced by one or several of the parameters to be estimated. Therefore, the parameters can be evaluated one by one in a designed sequence instead of together. In this way, a customized learning rate can be used for each parameter during the optimization, which ensures a fast and stable convergence. Besides, each parameter can be estimated with the impedance segment sensitive to it, which improves the estimation accuracy. The implementation of the proposed approach is elaborated and compared with a normal GD optimization-based approach. The results show that the proposed estimation approach has significantly higher accuracy and is more time efficient. Finally, the evaluated HPEVC's input impedance through the proposed approach is compared with the measured one to show the effectiveness of the established gray-box model.

The rest of this article is organized as follows. Section II introduces the impedance modeling of a typical charger's front-end converter. Section III discusses the influence of the design parameters on the charger's input impedance. Section IV discusses the challenges in a normal GD optimization-based approach and how they are addressed with the proposed approach. The implementation of the proposed parameter estimation algorithm is also presented. Section V shows the experiment carried out to verify the effectiveness of the proposed method. Finally, Section VI concludes this article.

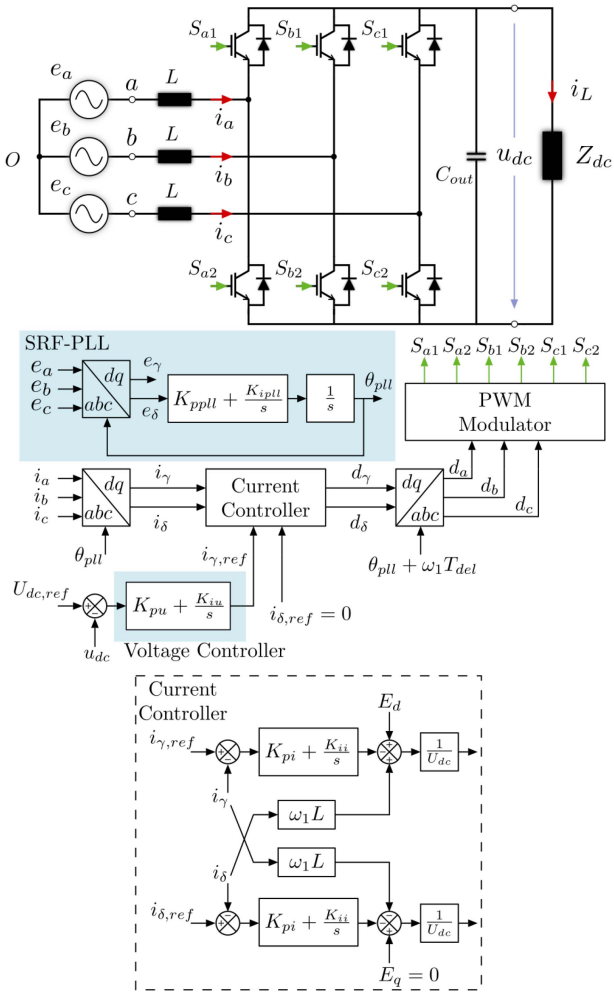

Fig. 1. Typical AFE converter of EV charger with the control block diagram.

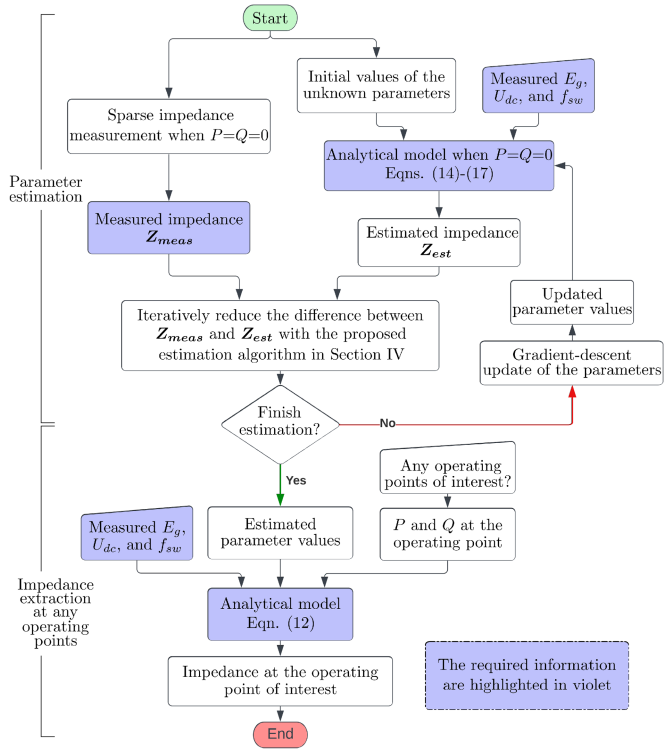

Fig. 2. Flowchart of the proposed gray-box modeling approach.

II. Overview and Impedance Modeling

A. System Description

An HPEVC usually consists of several parallel power modules with smaller power rating [22]. Each power module comprises a rectifier for the ac–dc conversion and a dc–dc converter. The rectifier dominates the HPEVC's input impedance of EV chargers since the dc–dc converter is decoupled by a large dc-link capacitor. The mainstream designs for the HPEVC's rectifier adopt either the Vienna rectifier or conventional active front end (AFE). Compared with the AFE, the Vienna rectifier has the same average model and normally has the same control strategy, except an additional mid-point voltage balancing control that does not influence the input impedance. Here, an AFE with a typical control shown in Fig. 1 is assumed to elaborate on the proposed approach. As seen, the control of the AFE consists of three loops, namely the synchronous reference frame phase-lock loop (SRF-PLL) for the grid synchronization, the grid current control loop in the synchronous reference frame, and the dc-link voltage control loop. Proportional-integral (PI) controllers are used as the regulators for all loops. The dc–dc converter after the AFE is simplified as an impedance $Z_{\rm dc}$. For clarity, the symbols with the subscripts d and q denote the variables in the dq frame synchronous to the grid voltage. In contrast, the symbols with the subscripts γ and δ denote the variables in the $\gamma\delta$ frame synchronous to the PLL angle $\theta_{\rm pll}$. The capital letters, e.g. E_d, denote the constants.

The analytical modeling of the AFE's input impedance has been well documented in the literature, which, however, requires the values of the design parameters. Among the required parameters, the amplitude of the grid voltage E_g, the dc-link voltage $u_{\rm dc}$, and the switching frequency $f_{\rm sw}$ of the AFE can be easily measured. However, due to confidentiality, the controller parameters, namely K_{ppll}, K_{ipll}, $K_{\rm pu}$, K_{iu}, K_{pi}, and K_{ii}, and the circuit parameters, namely L and $C_{\rm out}$ are unknown and cannot be measured directly. To extract the impedance in practice with confidential parameters, purely relying on measurement is unreliable because of the influence of measurement noises. Even when accurate measurement results are reachable, tremendous effort is still needed for measurements to obtain the impedance at different frequencies and operating points. Thus, a gray-box approach requiring less effort on measurement is proposed to extract the input impedance when the controller and circuit parameters shown in Fig. 1 are unknown.

B. Overview of the Proposed Approach

The flowchart of the proposed gray-box modeling approach is illustrated in Fig. 2. As seen, the whole approach consists of two stages, namely the parameter estimation stage and the impedance extraction stage. To estimate the controller and circuit parameters, the necessary information consists of the analytical impedance model, the measured impedance at sparse frequency points, and the measured E_g, $u_{\rm dc}$, and $f_{\rm sw}$. The controller and circuit parameters can be estimated by iteratively reducing the difference between the measured impedance $\boldsymbol{Z}_{\rm meas}$ and the

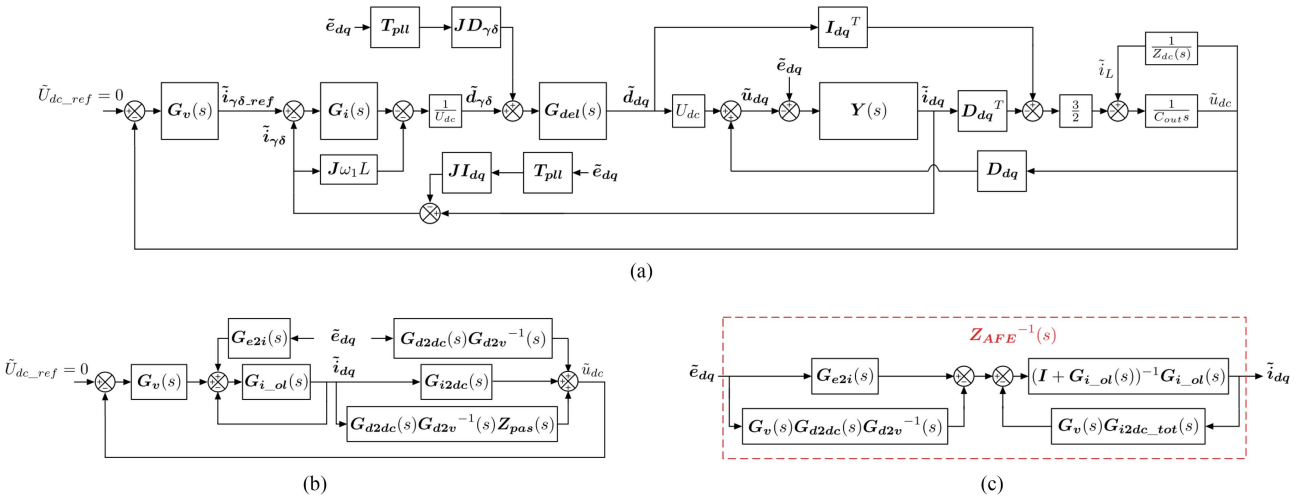

Fig. 3. (a) Small-signal model of the system. (b) Equivalent transformation I. (c) Equivalent transformation II.

estimated impedance $\boldsymbol{Z}_{\text{est}}$ through a GD optimization. To ensure accurate estimation results, a parameter estimation algorithm is proposed, which requires the impedance measured when the input active power P and the reactive power Q of the AFE are both zero. As elaborated in Section III, when $P = Q = 0$, the impedance is shaped by the parameters to be estimated in different frequency ranges so that the proposed estimation algorithm can be applied. Once the unknown parameters are estimated, the impedance at any operating points of interest can be easily extracted by using the analytical model.

Although the approach in Fig. 2 is proposed assuming the control system is the same as the one in Fig. 1, the proposed approach could still be effective when another control strategy is adopted if changing the analytical model to the corresponding one. As mentioned in [20], the impedance frequency response would be different if a different control method is used. Therefore, even though the exact control method is unknown in practice, the typical control strategies can be tried to find the one that results in the best match between $\boldsymbol{Z}_{\text{meas}}$ and $\boldsymbol{Z}_{\text{est}}$. Besides, as detailed in Section IV, an algorithm to obtain accurate estimation results is designed and implemented in the proposed gray-box modeling approach. When designing the estimation algorithm, one assumption used is that the multiple control loops are designed by following the well-known bandwidth selection design rule, which is choosing a higher bandwidth for the inner current loop whereas a lower bandwidth for the outer voltage loop. Although the design rule might not be adopted in every design, it is still followed by the majority in the industry because following the design rule saves much effort to properly design the control of an AFE. If the control of an AFE is designed without following the bandwidth selection rule, another estimation algorithm designed specifically is needed to identify the unknown parameters. However, this article focuses on the majority and the proposed estimation algorithm aims to be suitable for most AFEs.

C. Small-Signal Modeling

Based on the average model of the AFE and the control block diagram in Fig. 1, the block diagram of transfer matrices for the small-signal model of the AFE in the synchronous dq frame can be obtained. As shown in Fig. 3(a), the small signals are denoted by the symbols with a tilde, $\boldsymbol{G}_{\text{del}}(s)$ is the delay induced by the digital control and pulsewidth modulation (PWM) modulation, $\boldsymbol{Y}(\boldsymbol{s})$ is the admittance of the input L-filter, $\boldsymbol{G_v}(s)$ is the dc-link voltage controller, $\boldsymbol{G_i}(s)$ is the grid current controller without the dq current decoupling, $\boldsymbol{T}_{\text{pll}}(s)$ is the transfer matrix of the SRF-PLL [11], $\boldsymbol{J}$ is the equivalent matrix of the imaginary unit j [23], $\boldsymbol{J}\omega_1 L$ represents the dq current decoupling of the grid current controller. The details of the aforementioned transfer matrices are given in the Appendix, where T_{del}, which is the time delay caused by the digital control and PWM modulation, equals one and a half of the switching cycle period.

Additionally, in Fig. 3(a), an element denoted with the subscripts dq represents a vector consisting of the corresponding d-axis and q-axis variables, which applies to those with the subscripts $\gamma\delta$ as well. For example, (1) shows the details of the vector $\boldsymbol{D}_{\boldsymbol{\gamma\delta}}$ and $\tilde{\boldsymbol{u}}_{\boldsymbol{dq}}$ in Fig. 3(a)

$$\boldsymbol{D}_{\boldsymbol{\gamma\delta}} = \begin{bmatrix} D_\gamma \\ D_\delta \end{bmatrix}, \tilde{\boldsymbol{u}}_{\boldsymbol{dq}} = \begin{bmatrix} \tilde{u}_d \\ \tilde{u}_q \end{bmatrix}. \tag{1}$$

The model shown in Fig. 3(a) can be transformed into Fig. 3(b). The expressions of $\boldsymbol{G}_{\boldsymbol{d2}\text{dc}}(s)$, $\boldsymbol{G}_{\boldsymbol{d2v}}(s)$, $\boldsymbol{G}_{\boldsymbol{i2}\text{dc}}(s)$, and $\boldsymbol{Z}_{\text{pas}}(s)$ are given by

$$\boldsymbol{G}_{\boldsymbol{d2v}}(s) = U_{\text{dc}}\boldsymbol{I} + K(s)\boldsymbol{D}_{\boldsymbol{dq}}\boldsymbol{I}_{\boldsymbol{dq}}{}^T \tag{2}$$

$$\boldsymbol{G}_{\boldsymbol{i2}\text{dc}}(s) = K(s)\boldsymbol{D}_{\boldsymbol{dq}}^T \tag{3}$$

$$\boldsymbol{G}_{\boldsymbol{d2}\text{dc}}(s) = K(s)\boldsymbol{I}_{\boldsymbol{dq}}^T \tag{4}$$

$$\boldsymbol{Z}_{\text{pas}}(s) = \boldsymbol{Y}_{\text{pas}}{}^{-1}(s) = \boldsymbol{Y}^{-1}(s) + K(s)\boldsymbol{D}_{\boldsymbol{dq}}\boldsymbol{D}_{\boldsymbol{dq}}{}^T \tag{5}$$

where the expressions of $K(s)$ and $\boldsymbol{I}$ are given in the Appendix. Note that $Z_{\text{dc}}(s)$ can be simplified as a pure resistance.

The transfer matrix $\boldsymbol{G_{e2i}}(s)$ and the transfer matrix $\boldsymbol{G_{i\_ol}}(s)$ can be derived as

$$\begin{aligned}\boldsymbol{G_{e2i}}(s) = \boldsymbol{G_i}{}^{-1}(s)[U_{\text{dc}}\boldsymbol{G}_{\text{del}}{}^{-1}(s)\boldsymbol{G_{d2v}}{}^{-1}(s) \\ + (\boldsymbol{G_i}(s) - \boldsymbol{J}\omega_1 L)\boldsymbol{Y}_{\text{pll}}(s) - U_{\text{dc}}\boldsymbol{H}_{\text{pll}}(s)]\end{aligned} \tag{6}$$

$$\boldsymbol{G_{i\_ol}}(s) = (\boldsymbol{I} - \boldsymbol{H}(s)\boldsymbol{J}\omega_1 L)^{-1}\boldsymbol{H}(s)\boldsymbol{G_i}(s) \tag{7}$$

where

$$\boldsymbol{Y}_{\text{pll}}(s) = \boldsymbol{J}\boldsymbol{I}_{\boldsymbol{dq}}\boldsymbol{T}_{\text{pll}}(s) \tag{8}$$

$$\boldsymbol{H}_{\text{pll}}(s) = \boldsymbol{J}\boldsymbol{D}_{\boldsymbol{\gamma\delta}}\boldsymbol{T}_{\text{pll}}(s) \tag{9}$$

$$\boldsymbol{H}(s) = \frac{1}{U_{\text{dc}}}\boldsymbol{Y}_{\text{pas}}(s)\boldsymbol{G}_{\boldsymbol{d2v}}(s)\boldsymbol{G}_{\text{del}}(s). \tag{10}$$

The equivalent block diagram can be further transformed, as shown in Fig. 3(c). The expression of $\boldsymbol{G}_{\boldsymbol{i2}\text{dc\_tot}}(s)$ is given by

$$\boldsymbol{G}_{\boldsymbol{i2}\text{dc\_tot}}(s) = \boldsymbol{G}_{\boldsymbol{i2}\text{dc}}(s) + \boldsymbol{G}_{\boldsymbol{d2}\text{dc}}(s)\boldsymbol{G}_{\boldsymbol{d2v}}{}^{-1}(s)\boldsymbol{Z}_{\text{pas}}(s). \tag{11}$$

Finally, the impedance of the AFE can be written as

$$\boldsymbol{Z}_{\text{AFE}}(s) = (\boldsymbol{G}_{\boldsymbol{e2i}}(s) + \boldsymbol{G}_{\boldsymbol{v}}(s)\boldsymbol{G}_{\boldsymbol{d2}\text{dc}}(s)\boldsymbol{G}_{\boldsymbol{d2v}}{}^{-1}(s))^{-1} \times(\boldsymbol{I} + \boldsymbol{G}_{\boldsymbol{i}\_\text{ol}}{}^{-1}(s) + \boldsymbol{G}_{\boldsymbol{v}}(s)\boldsymbol{G}_{\boldsymbol{i2}\text{dc\_tot}}(s)). \tag{12}$$

D. Elements in the Impedance Matrix

The impedance is a two-by-two matrix, which is given by

$$\boldsymbol{Z}_{\text{AFE}}(s) = \begin{bmatrix} Z_{dd}(s) & Z_{dq}(s) \\ Z_{qd}(s) & Z_{qq}(s) \end{bmatrix}. \tag{13}$$

To prepare for the sensitivity study in Section III, the expressions of the $Z_{dd}(s)$, $Z_{dq}(s)$, $Z_{qd}(s)$, and $Z_{qq}(s)$ in (13) are derived. However, without simplification, the expressions of the four elements in the matrix $\boldsymbol{Z}_{\text{AFE}}(s)$ are too complicated. Nevertheless, from Fig. 3(a), it is noted that the expression can be significantly simplified when $I_d = I_q = D_q = 0$, i.e., $P = Q = 0$. When $P = Q = 0$, the simplified expressions of the four elements are given by (14)–(17)

$$Z_{dd\_0}(s) = (Ls + R)\cdot(1 + G_{i\_\text{ol\_siso}}(s)) \cdot(1 + G_{v\_\text{ol\_siso}}(s)) + \frac{3D_d^2}{2C_{\text{out}}s} \tag{14}$$

$$Z_{dq\_0}(s) = -\omega_1 L(1 - e^{-sT_{\text{del}}}) \tag{15}$$

$$Z_{qd\_0}(s) = \frac{\omega_1 L(1 - e^{-sT_{\text{del}}})}{1 - G_{\text{pll\_cl}}(s)\cdot e^{-sT_{\text{del}}}} \tag{16}$$

$$Z_{qq\_0}(s) = (Ls + R)\cdot\frac{1 + G_{i\_\text{ol\_siso}}(s)}{1 - G_{\text{pll\_cl}}(s)\cdot e^{-sT_{\text{del}}}} \tag{17}$$

where $G_{i\_\text{ol\_siso}}(s)$ and $G_{v\_\text{ol\_siso}}(s)$ are the open-loop transfer function of the current loop after the dq-axis decoupling [24] and the voltage loop, respectively. $G_{\text{pll\_cl}}$ is the closed-loop transfer function of the PLL [25]. The expressions of $G_{i\_\text{ol\_siso}}(s)$, $G_{v\_\text{ol\_siso}}(s)$, and $G_{\text{pll\_cl}}$ are given by

$$G_{i\_\text{ol\_siso}}(s) = \frac{(K_{pi}s + K_{ii})e^{-sT_{\text{del}}}}{s(Ls + R)} \tag{18}$$

$$G_{v\_\text{ol\_siso}}(s) = \frac{(K_{\text{pu}}s + K_{iu})}{s}\cdot\frac{3D_d}{2C_{\text{out}}s}\cdot G_{i\_\text{cl\_siso}}(s) = \frac{(K_{\text{pu}}s + K_{iu})}{s}\cdot\frac{3D_d}{2C_{\text{out}}s}\cdot\frac{G_{i\_\text{ol\_siso}}(s)}{1 + G_{i\_\text{ol\_siso}}(s)} \tag{19}$$

$$G_{\text{pll\_cl}}(s) = \frac{U_{\text{dc}}D_\gamma(K_{p\text{pll}}s + K_{i\text{pll}})}{E_d(K_{p\text{pll}}s + K_{i\text{pll}}) + s^2} \approx \frac{2\zeta\omega_{n\_\text{pll}}s + \omega_{n\_\text{pll}}^2}{s^2 + 2\zeta\omega_{n\_\text{pll}}s + \omega_{n\_\text{pll}}^2} \tag{20}$$

where $K_{p\text{pll}} = 2\zeta\omega_{n\_\text{pll}}/E_d$, $K_{i\text{pll}} = \omega_{n\_\text{pll}}^2/E_d$, and $U_{\text{dc}}D_\gamma \approx E_d$.

III. Impedance Sensitivity Study

A. Preconditioning

The previous section shows that the expression of $\boldsymbol{Z}_{\text{AFE\_0}}(s)$, which is the impedance of the AFE when $P = Q = 0$, is a function given by

$$\boldsymbol{Z}_{\text{AFE\_0}}(s) = f(R, L, K_{pi}, K_{ii}, K_{p\text{pll}}, K_{i\text{pll}} K_{\text{pu}}, K_{iu}, f_{\text{sw}}, E_d, U_{\text{dc}}, C_{\text{out}}). \tag{21}$$

As mentioned in Section II-A, f_{sw}, E_d, and U_{dc} can be easily measured. Thus, the estimation of the three parameters is unnecessary, and their influence on the impedance will be not discussed. Besides, the impact of R, i.e., the equivalent loss resistance of the AFE, to $\boldsymbol{Z}_{\text{AFE}}(s)$ is found negligible in the typical range, i.e., $< 500\ m\Omega$. Thus, R is also not estimated. Instead, a typical value, i.e., $200\ m\Omega$, is assumed for R in the gray-box modeling of an AFE, which leads to minor errors.

The rest eight parameters, i.e., L, C_{out}, and the controller parameters, will be estimated. As aforementioned, a multiparameter estimation problem generally results in a nonconvex optimization problem, which can suffer from low estimation accuracy because of the existence of saddle points.

Thus, we analyze the sensitivity of the impedance to the variation of each parameter to be estimated. As shown later, the sensitivity study reveals that different parameters can shape the impedance until different frequencies. Therefore, an estimation sequence for the eight parameters can be defined. In this way, the multiparameter estimation problem can be cast into several one-parameter estimation problems to improve accuracy.

B. Influential Frequency Range Per Parameter

According to (14)–(17), except for Z_{dq_0}, the impedance elements Z_{dd_0}, Z_{qd_0}, and Z_{qq_0} are shaped by not only the passive components but also the control loop of the AFE.

However, the influence of the control loop is limited to a frequency that is positively related to the corresponding loop bandwidth. For instance, in (14), the item $1 + G_{v\_\text{ol\_siso}}$ can be approximated as 1 when $|G_{v\_\text{ol\_siso}}| \ll 1$ at frequencies far above the bandwidth of the VL. Similarly, $G_{i\_\text{ol\_siso}}$ can also be neglected when $|G_{i\_\text{ol\_siso}}| \ll 1$. As for Z_{qd_0} and Z_{qq_0}, they are shaped only by the PLL regulator parameters. As the same, the closed-loop transfer function $G_{\text{pll\_cl}}$ of the PLL can be ignored at high frequencies where $|G_{\text{pll\_cl}}| \ll 1$.

To reduce the effort of designing the control loops, some standard rules [24], [26] are followed to obtain satisfying dynamic performances, a stable system with enough margin, and a narrow frequency region of the negative input impedance [10], [11], [27], which leads to enough gain and phase margin for

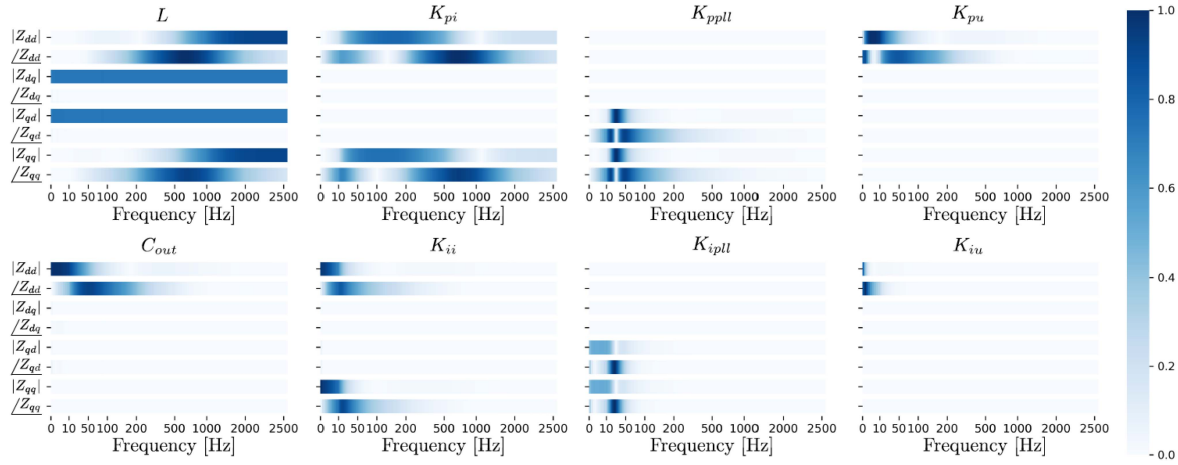

Fig. 4. Partial derivative of the magnitude and phase of Z_{dd}, Z_{dq}, Z_{qd}, Z_{qq} w.r.t each parameter at the value given in Table II. Note that the frequency is given in the synchronous dq-frame.

TABLE II
PARAMETERS OF CHARGER'S AFE

Symbol	Description	Value
U_{dc}	AFE output dc voltage	385 V
E_g	Grid line-neutral peak voltage	$110\sqrt{2}$ V
ω_1	Grid frequency	$2\pi\times50$ rad/s
f_{sw}	Switching frequency of AFE	20 kHz
C_{out}	Output capacitance of AFE	1.67 mF
L	Inductance of AFE	2.5 mH
K_{pi}	Proportional gain of current controller	9
K_{ii}	Integral gain of current controller	1000
K_{ppll}	Proportional gain of PLL	1.21
K_{ipll}	Integral gain of PLL	228.40
K_{pu}	Proportional gain of voltage controller	0.2
K_{iu}	Integral gain of voltage controller	2
BW_{CL}	Bandwidth of current control loop	1 kHz
BW_{PLL}	Bandwidth of PLL	50 Hz
BW_{VL}	Bandwidth of voltage control loop	30 Hz

stability but limited loop bandwidths. Typically, for an AFE, a bandwidth above 200 Hz is used for the CL so that the current response is fast [26]. Furthermore, the bandwidth of the outer VL is generally ten to 20 times lower than the bandwidth of the inner CL, which generally results in a VL bandwidth below 100 Hz [26], [28], [29]. Such a bandwidth selection makes the tuning of the control easier by decoupling the inner loop and outer loop [26]. Furthermore, a bandwidth below 100 Hz is generally used for PLLs to prevent instabilities and attenuate the grid voltage noise [25], [30]. As long as the bandwidth of the CL, VL, and PLL is selected as aforementioned, the influential frequency range of each parameter will not change or have only marginal change. Such stems from the fact that the influence of the parameters on the impedance is determined by the bandwidth of the corresponding control loops, which is revealed by (14)–(17).

A case study is carried out to elaborate on the influential frequency range of the parameters. The parameters of the AFE in the case study are given in Table II.

Fig. 4 shows the absolute value of the partial derivative of $|Z_x|$ and $\angle Z_x$ w.r.t. each parameter, where x represents dd_0, dq_0, qd_0, qq_0. Note that the results are normalized for each parameter. With a darker blue, it indicates that $|Z_x|$ and $\angle Z_x$ are influenced by a parameter more at these frequencies than at the other frequencies. On the contrary, a zero partial derivative means no influence on $|Z_x|$ and $\angle Z_x$. Note that similar results with marginal differences can be obtained when the parameters are different as long as the bandwidths of the control loops are designed reasonably as aforementioned.

Clearly, $|Z_{dd\_0}|$ and $|Z_{qq\_0}|$ above the CL bandwidth are mainly shaped by L. $|Z_{dq\_0}|$ is only determined by L but not by other parameters, which confirms (15). C_{out} has influence on $\angle Z_{dd\_0}$ and $|Z_{dd\_0}|$ mainly below the VL bandwidth. As for the controller parameters, it is noted that the proportional gains shape the impedance in broader frequency ranges than their corresponding integral gains, which is reasonable for PI controllers. Besides, their influences on the impedance elements Z_{dd_0,dq_0,qd_0,qq_0} are limited by their corresponding loop bandwidth.

The observation in Fig. 4 matches the analytical expressions given by (14)–(17). The analysis indicates that the impedance is sensitive to the variation of a parameter only in a frequency range, which is determined by the corresponding loop bandwidth. Besides, Fig. 4 and (14)–(17) both reveals that Z_{dd_0} is not shaped by K_{ppll} and K_{ipll}. Besides, Z_{dq_0} is only influenced by L. Finally, Z_{qq_0} is not shaped by K_{pu}, K_{iu}, and C_{out}.

IV. MULTIPLE PARAMETER ESTIMATION

As aforementioned, the parameter estimation problem is essentially an optimization problem, which can be solved with GD methods. When the parameters are correctly estimated, the magnitude and phase of the estimated impedance $\boldsymbol{Z}_{\text{AFE\_est}}(s)$ should optimally match with the measured impedance $\boldsymbol{Z}_{\text{AFE\_meas}}(s)$. Therefore, the loss function is given by

$$f_{\text{loss}} = \frac{1}{2M}\sum\left[\frac{1}{N}\sum_{i=1}^{N}\left[\left(|Z_{e\_\text{est}}(f_i)| - |Z_{e\_\text{meas}}(f_i)|\right)^2 + \left(\angle Z_{e\_\text{est}}(f_i) - \angle Z_{e\_\text{meas}}(f_i)\right)^2\right]\right] \tag{22}$$

where e represents dd, dq, qd, qq, f_i is the ith frequency point of the impedance measurement, N is the total number of the

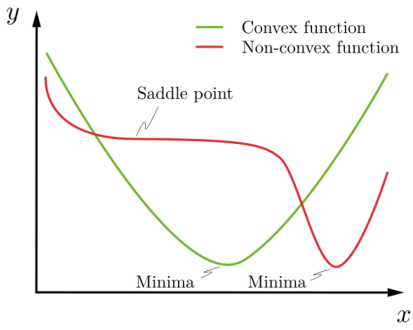

Fig. 5. Saddle points in a nonconvex function.

frequency points in the impedance measurement, M is the number, which is maximally four, of the impedance elements composing the loss function. During the optimization process, a learning rate is decided for the optimizer to update all parameters under estimation iteratively. The loss value will decrease because a GD direction is calculated to update the parameters.

A. Challenges in a Normal GD Optimization-Based Approach

Two challenges, namely low estimation accuracy and high time cost, can arise when using GD optimization to estimate the parameters. These issues are caused by two reasons.

The first reason is the significant difference in the scaling of the parameters, because of their different unit. Different scaling indicates that each parameter requires a different learning rate to achieve fast and stable convergence. If the learning rate is too small for a parameter, the loss value will converge too slowly. If the learning rate is too big, the loss value will bounce between the minima. Therefore, due to the scaling difference, using the same learning rate for all parameters can result in either a huge time cost for the estimation or an inaccurate estimation result, or both.

The second reason is the loss function given by (22) is nonconvex since its Hessian matrix is not positive semidefinite. Such increases the difficulties in converging to the minima because of the existence of the saddle points [21]. As depicted in Fig. 5, when the loss function is nonconvex, there are saddle points in the function. Because of the zero gradients there, these saddle points will slow down the optimization and get the optimization stuck in the worst cases. The existence of saddle points increases the time needed for converging to the minima tremendously and decreases the estimation accuracy, if the optimization gets stuck [21], [31].

B. Proposed Estimation Approach

The challenges faced by the normal GD optimization-based estimation can be addressed by estimating the parameters separately. In this way, a multiparameter estimation problem is cast as several one-parameter estimation problems, which reduces the dimension of the optimization problem. Thus, the customized learning rate can be used for the estimation of different parameters.

However, since the impedance is determined by all parameters together, if one parameter stays at an incorrect value, the others cannot be estimated correctly. Updating the parameters iteratively to approach the correct values may solve the problem. Nevertheless, it increases the time cost tremendously.

A more efficient estimation approach is needed. As the sensitivity study in Section III reveals, although the impedance is determined by all of the eight parameters to be estimated at low frequencies, the impedance is influenced by only one or several of them at higher frequencies. Besides, as both Fig. 4 and (14)–(17) reveal, instead of all of the eight parameters, only one or several of them have influences, for each impedance element among Z_{dd_0}–Z_{qq_0}. Therefore, an estimation sequence of the parameters can be defined to effectively evaluate the eight parameters one by one.

Besides, as discussed in Section III and shown in Fig. 4, for a certain parameter, the impedance is more sensitive to its variation at some frequencies. When estimating the parameter, if the corresponding sensitive segment of impedance is used to compose the loss function, the saddle point issue can be avoided. At saddle points, the gradient of the loss function is zero but the loss value is still high. However, if the sensitive segment of impedance is used to compose the loss function, the gradient is zero only when the loss value is zero. For clarity, the gradient of the loss function (22) w.r.t. a parameter x is derived, which is obtain as

$$\frac{\partial f_{\text{loss}}}{\partial x} = \frac{1}{M}\sum\left[\frac{1}{N}\sum_{i=1}^{N}\left[(|Z_{e\_\text{est}}(f_i)| - |Z_{e\_\text{meas}}(f_i)|)\frac{\partial |Z_{e\_\text{est}}(f_i)|}{\partial x} + (\angle Z_{e\_\text{est}}(f_i) - \angle Z_{e\_\text{meas}}(f_i))\frac{\partial \angle Z_{e\_\text{est}}(f_i)}{\partial x}\right]\right]. \quad (23)$$

As seen, when the sensitive impedance segment is selected, $\partial|Z_{e\_\text{est}}(f_i)|/\partial x \neq 0$ and $\partial\angle Z_{e\_\text{est}}(f_i)/\partial x \neq 0$. Thus, $\partial f_{\text{loss}}/\partial x = 0$ only when $|Z_{e\_\text{est}}(f_i)| = |Z_{e\_\text{meas}}(f_i)|$ and $\angle Z_{e\_\text{est}}(f_i) = \angle Z_{e\_\text{meas}}(f_i)$, which means the loss value is zero.

Based on the analysis above and the sensitivity study in Section III, a time-efficient estimation algorithm, which also improves the estimation accuracy, is proposed. The flowchart of the algorithm is illustrated in Fig. 6. As shown in Fig. 6(a), the impedance measured at $P = Q = 0$ is used for the parameter estimation, and the parameters are estimated in sequence.

The reasoning for why the algorithm is designed as such is as follows. To start with, (15) reveals that Z_{dq_0} is only influenced by L. So, L can be estimated first using $|Z_{dq\_0}|$ to compose its loss function. However, only the $|Z_{dq\_0}|$ above 2 kHz is used because the measured $|Z_{dq\_0}|$ at low frequency is inaccurate. Because of the higher bandwidth of the CL than the VL and PLL bandwidth, K_{pi} shapes the impedance until higher frequencies compared with the rest parameters. Thus, K_{pi} is identified next. Since the CL bandwidth is typically higher than 200 Hz, the measured $|Z_{dd}|$, $|Z_{qq}|$, $\angle Z_{dd}$, and $\angle Z_{qq}$ above 200 Hz should be used to identify K_{pi}. Here, the impedance measured between 200 and 1000 Hz is used for the K_{pi} estimation.

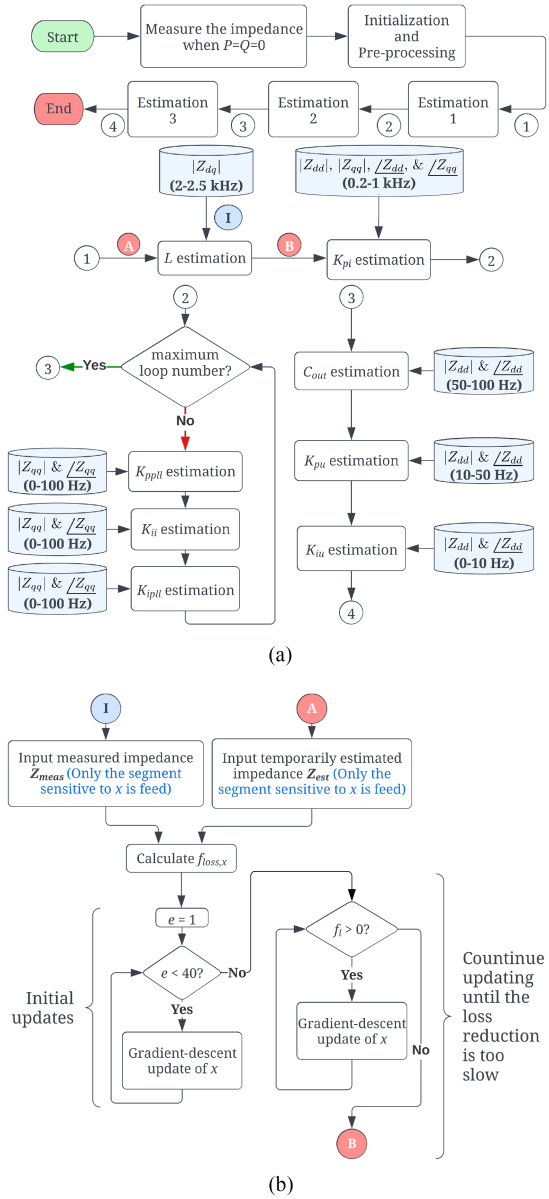

Fig. 6. (a) Flowchart of the estimation algorithm. (b) Flowchart of the estimation of the parameter x, where e represents the number of epochs, and the expression of f_l is given by (24).

Furthermore, as revealed by (17) and visualized in Fig. 4, Z_{qq_0} is only influenced by K_{ii}, $K_{p\text{pll}}$, and $K_{i\text{pll}}$. Their influential frequency range is typically within 100 Hz, which is determined by the commonly followed design rules, e.g., bandwidth and phase margin selections for the PLL and the CL. Thus, Z_{qq_0} measured below 100 Hz is used to identify the three parameters. However, their influential frequency ranges are similar to each other. When identifying one of the three, e.g., $K_{p\text{pll}}$, the estimated value could be far away from the exact one when K_{ii} and $K_{i\text{pll}}$ stay at the wrong values. Thus, a loop is created to identify them iteratively. In this way, the three parameters can approach the correct values gradually and which parameter is estimated first does not make a difference. After several cycles, which is 5 cycles in our case, the loop is ended because the values of the three parameters do not change significantly. Although the cycle number that should be used in another scenario could be different, it can be easily decided by observing if the three parameters' values change significantly or not after a certain number of cycles.

TABLE III
ELEMENTS AND FREQUENCY RANGE OF THE IMPEDANCE DATA USED TO COMPOSE THE LOSS FUNCTIONS

Parameter	Elements	Frequency range
L	$\lvert Z_{dq}\rvert$	(2-2.5 kHz)
K_{pi}	$\lvert Z_{dd}\rvert$, $\lvert Z_{qq}\rvert$, $\angle Z_{dd}$, and $\angle Z_{qq}$	(0.2-1 kHz)
$K_{p\text{pll}}$	$\lvert Z_{qq}\rvert$ and $\angle Z_{qq}$	(0-100 Hz)
K_{ii}	$\lvert Z_{qq}\rvert$ and $\angle Z_{qq}$	(0-100 Hz)
$K_{i\text{pll}}$	$\lvert Z_{qq}\rvert$ and $\angle Z_{qq}$	(0-100 Hz)
C_{out}	$\lvert Z_{dd}\rvert$ and $\angle Z_{dd}$	(50-100 Hz)
K_{pu}	$\lvert Z_{dd}\rvert$ and $\angle Z_{dd}$	(10-50 Hz)
K_{iu}	$\lvert Z_{dd}\rvert$ and $\angle Z_{dd}$	(0-10 Hz)

Finally, K_{pu}, K_{iu}, and C_{out} can be estimated with Z_{dd_0} measured below 100 Hz, which is determined by the VL bandwidth. Furthermore, as revealed by Fig. 4 and discussed in Section III, K_{iu} can shape Z_{dd_0} until a lower frequency than the K_{pu} and C_{out}. Thus, K_{iu} is identified after K_{pu} and C_{out}. As for K_{pu} and C_{out}, their influential frequency ranges are similar to each other. Any one of the two can be estimated first as long as the measured impedance at relatively higher frequencies is used to identify the parameter. For instance, C_{out} can be estimated first by using the measured impedance between 50 and 100 Hz. Afterward, K_{pu} can be estimated with the measured impedance between 10 and 50 Hz. However, the estimation results do not change significantly if K_{pu} is estimated first by using the measured impedance between 50 and 100 Hz.

In summary, the impedance elements and the frequency ranges of the impedance segment selected to compose the loss function for the estimation of each parameter are shown in Table III. Additionally, several points as follows are worth mentioning.

1) L and C_{out} can be initialized randomly.
2) The proportional gain and the integral gain for all controllers should be initially low so that they can be estimated with the designed order.
3) The GD optimizer Adam [32] is utilized to update the parameter iteratively, which leads to a fast and stable convergence.
4) The magnitude and phase of the measured impedance element should be normalized, and the same transformation should be applied to the estimated impedance elements.

In Fig. 6(b), the flowchart of the estimation for each parameter is shown. As seen, a variable f_l is calculated to determine when the estimation of the parameter should stop. The expression of f_l is given by

$$f_l = \Delta f_{\text{loss}}[-1] - \Delta f_{\text{loss}}[0]/10 \tag{24}$$

where $\Delta f_{\text{loss}}[-1]$ is the loss reduction in the last 20 epochs, whereas $\Delta f_{\text{loss}}[0]$ is the loss reduction in the first 20 epochs. The reason for using f_l instead of a defined loss value limit

Algorithm 1: Estimation Per Parameter x.

Initialization:
Make parameter x as a variable
Keep the other parameters as constants
Input the corresponding loss function $f_{loss,x}$

Initial updates:
for $(e = 0; e < 40; e++)$**:**
$g = \frac{\partial f_{loss,x}}{\partial x}$
Update x with *Adam* optimizer in the opposite direction of g
Update $\boldsymbol{Z_{est}}$ with (14)–(17) and apply the normalization
Update $f_{loss,x}$
end for

Continue updating:
Calculate f_l with (24)
while $(f_l > 0)$**:**
$g = \frac{\partial f_{loss,x}}{\partial x}$
Update x with *Adam* optimizer in the opposite direction of g
Update $\boldsymbol{Z_{est}}$ with (14)–(17) and apply the normalization
Update $f_{loss,x}$
Update f_l with (24)
end while

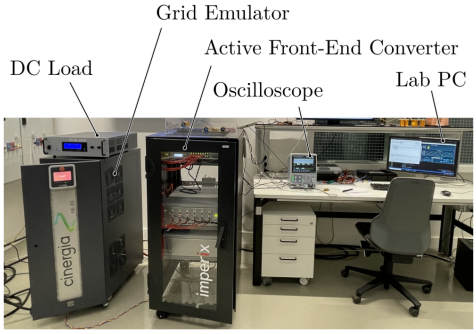

Fig. 7. Impedance measurement setup.

to stop the estimation is as follows. Since Adam optimizer is used for the optimization, an adaptive learning rate is used when updating the parameter's value, which results in a slow reduction of the loss value when approaching the minimum. Therefore, it requires a proper loss value limit with which a balance between the estimation accuracy and the time cost is achieved. However, such a proper loss value limit changes from case to case, which is dependent on the measurement errors and the impedance data used to compose the loss function. Thus, f_l is calculated to determine whether the loss value reduction is too slow. As aforementioned, when the loss value reduction is slow, it indicates that the loss value is close to the minimum. Therefore, as illustrated in Fig. 6(b), the estimation of the parameter stops when $f_l < 0$, which achieves the tradeoff between the estimation accuracy and the time cost. In summary, the pseudocode of the estimation algorithm is shown in Algorithms 1 and 2.

V. Experimental Results

A. Experiments and Measurement Setup

The experiment setup is shown in Fig. 7. As seen, a Cinergia grid emulator is used to generate the grid voltage and inject harmonic voltages. An imperix power test bench is used to mimic an AFE. The imperix power test bench has a programmable controller, six 2.5 mH inductors, and six power modules. Thus, much flexibility is provided to change the AFE's design specifications. The adjustable dc load is connected to the output of the emulated AFE for different operating power. The current

Algorithm 2: Parameter Estimation.

Initialization & pre-processing:
Prepare the impedance data measured when $P = Q = 0$
Normalize the magnitude and phase of $\boldsymbol{Z_{meas}}$
Initialize L, K_{pi}, K_{ii}, K_{ppll}, K_{ipll}, K_{pu}, and K_{iu}
Input the measured E_g, U_{dc}, and f_{sw}
Calculate $\boldsymbol{Z_{est}}$ with (14)–(17) and apply the normalization

L **estimation:**
$Z_1 = \{Z_{dq\_est}(f_i)\}$, $f_i \in$ (2–2.5 kHz)
$Z_2 = \{Z_{dq\_meas}(f_i)\}$, $f_i \in$ (2–2.5 kHz)
$f_{loss,L} = \frac{1}{N}\sum_{i=1}^{N}(|Z_1| - |Z_2|)^2$
Optimize $f_{loss,L}$ by updating L with **Algorithm 1**

K_{pi} **estimation:**
$Z_1 = \{Z_{dd\_est}(f_i), Z_{qq\_est}(f_i)\}$, $f_i \in$ (0.2–1 kHz)
$Z_2 = \{Z_{dd\_meas}(f_i), Z_{qq\_meas}(f_i)\}$, $f_i \in$ (0.2–1 kHz)
$f_{loss,Kpi} = \frac{1}{N}\sum_{i=1}^{N}[(|Z_1| - |Z_2|)^2 + (\angle Z_1 - \angle Z_2)^2]$
Optimize $f_{loss,Kpi}$ by updating K_{pi} with **Algorithm 1**

Define a maximum loop number n_1
for $(i = 0; i < n_1; i++)$**:**
K_{ppll} **estimation:**
$Z_1 = \{Z_{qq\_est}(f_i)\}$, $f_i \in$ (0–100 Hz)
$Z_2 = \{Z_{qq\_meas}(f_i)\}$, $f_i \in$ (0–100 Hz)
$f_{loss,Kppll} = \frac{1}{N}\sum_{i=1}^{N}[(|Z_1| - |Z_2|)^2 + (\angle Z_1 - \angle Z_2)^2]$
Optimize $f_{loss,Kppll}$ by updating K_{ppll} with **Algorithm 1**
K_{ii} **estimation:**
$Z_1 = \{Z_{qq\_est}(f_i)\}$, $f_i \in$ (0–100 Hz)
$Z_2 = \{Z_{qq\_meas}(f_i)\}$, $f_i \in$ (0–100 Hz)
$f_{loss,Kii} = \frac{1}{N}\sum_{i=1}^{N}[(|Z_1| - |Z_2|)^2 + (\angle Z_1 - \angle Z_2)^2]$
Optimize $f_{loss,Kii}$ by updating K_{ii} with **Algorithm 1**
K_{ipll} **estimation:**
$Z_1 = \{Z_{qq\_est}(f_i)\}$, $f_i \in$ (0–100 Hz)
$Z_2 = \{Z_{qq\_meas}(f_i)\}$, $f_i \in$ (0–100 Hz)
$f_{loss,Kipll} = \frac{1}{N}\sum_{i=1}^{N}[(|Z_1| - |Z_2|)^2 + (\angle Z_1 - \angle Z_2)^2]$
Optimize $f_{loss,Kipll}$ by updating K_{ipll} with **Algorithm 1**
end for

C_{out} **estimation:**
$Z_1 = \{Z_{dd\_est}(f_i)\}$, $f_i \in$ (50–100 Hz)
$Z_2 = \{Z_{dd\_meas}(f_i)\}$, $f_i \in$ (50–100 Hz)
$f_{loss,Cout} = \frac{1}{N}\sum_{i=1}^{N}[(|Z_1| - |Z_2|)^2 + (\angle Z_1 - \angle Z_2)^2]$
Optimize $f_{loss,Cout}$ by updating C_{out} with **Algorithm 1**

K_{pu} **estimation:**
$Z_1 = \{Z_{dd\_est}(f_i)\}$, $f_i \in$ (10–50 Hz)
$Z_2 = \{Z_{dd\_meas}(f_i)\}$, $f_i \in$ (10–50 Hz)
$f_{loss,Kpu} = \frac{1}{N}\sum_{i=1}^{N}[(|Z_1| - |Z_2|)^2 + (\angle Z_1 - \angle Z_2)^2]$
Optimize $f_{loss,Kpu}$ by updating K_{pu} with **Algorithm 1**

K_{iu} **estimation:**
$Z_1 = \{Z_{dd\_est}(f_i)\}$, $f_i \in$ (0–10 Hz)
$Z_2 = \{Z_{dd\_meas}(f_i)\}$, $f_i \in$ (0–10 Hz)
$f_{loss,Kiu} = \frac{1}{N}\sum_{i=1}^{N}[(|Z_1| - |Z_2|)^2 + (\angle Z_1 - \angle Z_2)^2]$
Optimize $f_{loss,Kiu}$ by updating K_{iu} with **Algorithm 1**

TABLE IV
THREE DESIGNS USED IN THE EXPERIMENT

Parameter	Design 1	Design 2	Design 3
L [mH]	2.5	2.5	1.25
K_{pi}	9	15.7	1.57
K_{ppll}	1.21	4	2.42
K_{ii}	1000	15297	306
K_{ipll}	228	634	914
C_{out} [mF]	1.67	1.67	3.21
K_{pu}	0.2	0.43	0.33
K_{iu}	2	10.47	4.66

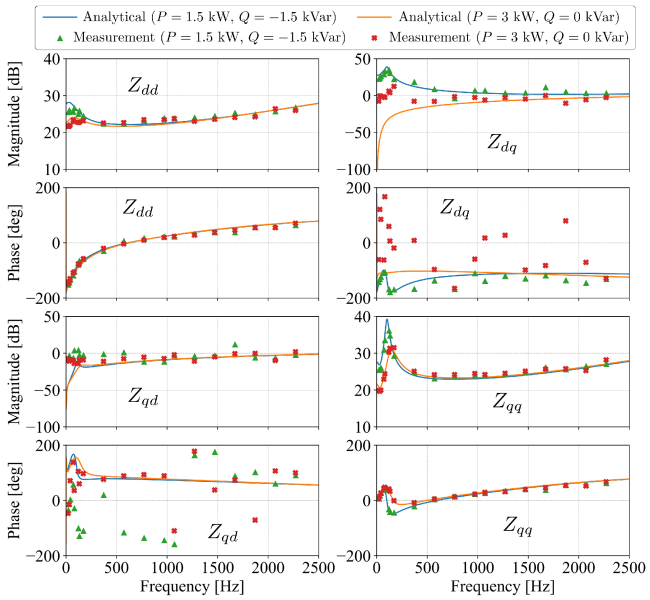

Fig. 8. Measured impedance of the AFE with Design 2 specifications at two operating points. The analytical results are also shown for a comparison to verify the correctness of the derived analytical model.

probes, the voltage probes, and the scope used in the experiments are Yokogawa 701933, Keysight N2791 A, and Yokogawa DLM2034, respectively.

As shown in Table IV, three groups of immeasurable parameters are used in the experiment to account for parameter uncertainty. As for the measurable parameters U_{dc}, E_g, and f_{sw}, they are the same for the three designs and given in Table II.

B. Analytical Model Verification

In Fig. 8, the measured impedance of the AFE with Design 2 specifications at two operating points is compared with the analytical model. As seen, for Z_{dd} and Z_{qq}, the measurement results match the analytical calculation results. For the coupling impedance Z_{dq} and Z_{qd}, there are significant mismatches. The mismatches are caused by measurement errors that stem from the low magnitude of the coupling impedance. When the magnitude of the coupling impedance is enough high to be comparable to $|Z_{dd}|$ and $|Z_{qq}|$, the analytical results match the measurement results. As seen in Fig. 8, when the power factor is lower, $|Z_{dq}|$ is higher. Furthermore, for both $|Z_{dq}|$ and $\angle Z_{dq}$, the analytical results match the measured ones. To further explain why the mismatches exist when $|Z_{dq}|$ and $|Z_{qd}|$ are low, the reasoning is as follows. When measuring the input impedance, grid voltage perturbations at f_p are injected. Then, input voltages $u_{abc}(t)$ and currents $i_{abc}(t)$ of the AFE are measured. Furthermore, $u_{abc}(t)$ and $i_{abc}(t)$ are rotated to the same dq-frame resulting in $u_{dq}(t)$ and $i_{dq}(t)$, respectively. The grid frequency is f_1. By applying fast Fourier transform (FFT), the $f_p - f_1$ frequency component in $u_{dq}(t)$ and $i_{dq}(t)$ can be extracted resulting in $U_{dq}(f_p - f_1) = U_d e^{j\phi_{dv}} + jU_q e^{j\phi_{qv}}$ and $I_{dq}(f_p - f_1) = I_d e^{j\phi_{di}} + jI_q e^{j\phi_{qi}}$, respectively. Therefore, (25) is satisfied. Similarly, grid voltage perturbations at $2f_1 - f_p$ are injected to obtain $U'_d e^{j\phi'_{dv}}$, $U'_q e^{j\phi'_{qv}}$, $I'_d e^{j\phi'_{di}}$, and $I'_q e^{j\phi'_{qi}}$, which satisfy (26). Finally, the impedance at $f_p - f_1$ can be calculated from (25) and (26), because $\boldsymbol{Z}_{\text{AFE}}(\boldsymbol{f}) = \boldsymbol{Z}^*_{\text{AFE}}(-\boldsymbol{f})$ [11], where the superscript $*$ indicates the conjugate complex form of the original variable

$$\begin{cases} U_d e^{j\phi_{dv}} = Z_{dd}(f) I_d e^{j\phi_{di}} + Z_{dq}(f) I_q e^{j\phi_{qi}}, f = f_p - f_1 \\ U_q e^{j\phi_{qv}} = Z_{qd}(f) I_d e^{j\phi_{di}} + Z_{qq}(f) I_q e^{j\phi_{qi}}, f = f_p - f_1 \end{cases} \tag{25}$$

$$\begin{cases} U'_d e^{j\phi'_{dv}} = Z_{dd}(f) I'_d e^{j\phi'_{di}} + Z_{dq}(f) I'_q e^{j\phi'_{qi}}, f = f_1 - f_p \\ U'_q e^{j\phi'_{qv}} = Z_{qd}(f) I'_d e^{j\phi'_{di}} + Z_{qq}(f) I'_q e^{j\phi'_{qi}}, f = f_1 - f_p \end{cases} \tag{26}$$

However, when $|Z_{dq}(f)| \ll |Z_{dd}(f)|$ and $|Z_{qd}(f)| \ll |Z_{qq}(f)|$, the $Z_{dq}(f)$ and $Z_{qd}(f)$ calculated from the measured voltages and currents are extremely sensitive to measurement noises. As seen from the first equation in (25), when $|Z_{dd}(f)| \gg |Z_{dq}(f)|$, $Z_{dd}(f) I_d e^{j\phi_{di}} \gg Z_{dq}(f) I_q e^{j\phi_{qi}}$ because I_d and I_q have comparable scaling. Therefore, any tiny measurement errors of $U_d e^{j\phi_{dv}}$, $I_d e^{j\phi_{di}}$, and $I_q e^{j\phi_{qi}}$, e.g., 10 mV or 10 mA, can result in a significant error in the calculated $Z_{dq}(f)$. Similarly, when $|Z_{qq}|(f) \gg |Z_{qd}|(f)$, $Z_{qd}(f)$ calculated from the measured voltages and currents also has significant errors. Thus, when $|Z_{dq}(f)|$ and $|Z_{qd}(f)|$ are much smaller than $|Z_{dd}(f)|$ and $|Z_{qq}(f)|$, the measured coupling impedance is unreliable. As revealed later, such an issue of inaccurate measurement can be addressed by the proposed gray-box modeling approach.

C. Estimation Results

Following the flow in Fig. 2, the input impedance of the charger at $P = Q = 0$ should be measured firstly for the parameter estimation. The data used for the parameter estimation for the three designs are visualized in Fig. 9. As seen, the analytical calculation results are also shown for comparison. In total, 54 frequency points are measured for each design to estimate the unknown parameters.

Fig. 10 shows the loss values and parameter updates during the evaluation progress. For all designs and all parameters, the loss value decreases during the estimation. Besides, the estimated parameter values approach the exact one gradually. The final estimation results are provided in Table V. Besides, Table V compares the performance of the proposed method with the performance of the normal GD optimization-based approach. In the normal approach, all parameters are estimated simultaneously with the same data set, the same GD optimizer, the same number

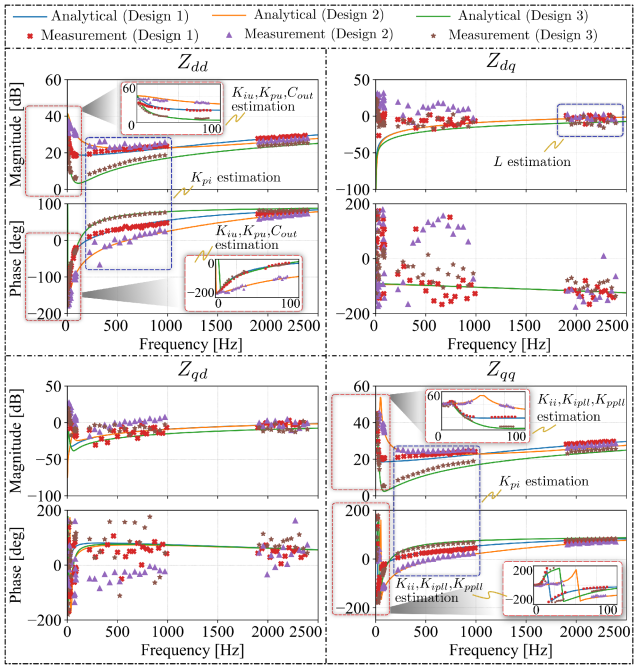

Fig. 9. The impedance measured at $P = Q = 0$, which is used for parameter estimation. The analytical calculation results are shown for comparison.

of total epochs for the estimation, and the same initialization values as those in the proposed approach. However, without the proposed estimation algorithm in the normal approach, the optimization easily gets stuck at saddle points resulting in high errors in the identified parameter values. Moreover, the time to finish the same number of epochs is about three times higher than the one needed in the proposed approach. This is because the whole dataset is used in the normal approach, whereas in the proposed approach only the sensitive impedance segment is used for the optimization. Therefore, the proposed approach has less amount of data for calculation in each epoch resulting in less time cost.

In both Fig. 10 and Table V, it is noted that some identified parameter values have high errors. Such errors are caused by the insensitivity of the impedance to those parameters. Depending on the design specifications, the impedance could become less sensitive to one or several parameters, and thereby low estimation accuracy is seen for those parameters. For instance, in Table V, for Design 1, K_{iu} has the highest estimation error whereas K_{ii} has the highest error for Design 3. However, since the impedance is less sensitive to these parameters, their high estimation errors would not result in significant errors in the estimated impedance and thereby are not problematic. The analytical impedance calculated with the estimation results shown in Table V is illustrated in Fig. 11. As seen, despite some errors in the identified parameter values, the estimated impedance has high accuracy. However, significant errors are noticed in the impedance estimated via the normal GD optimization-based approach.

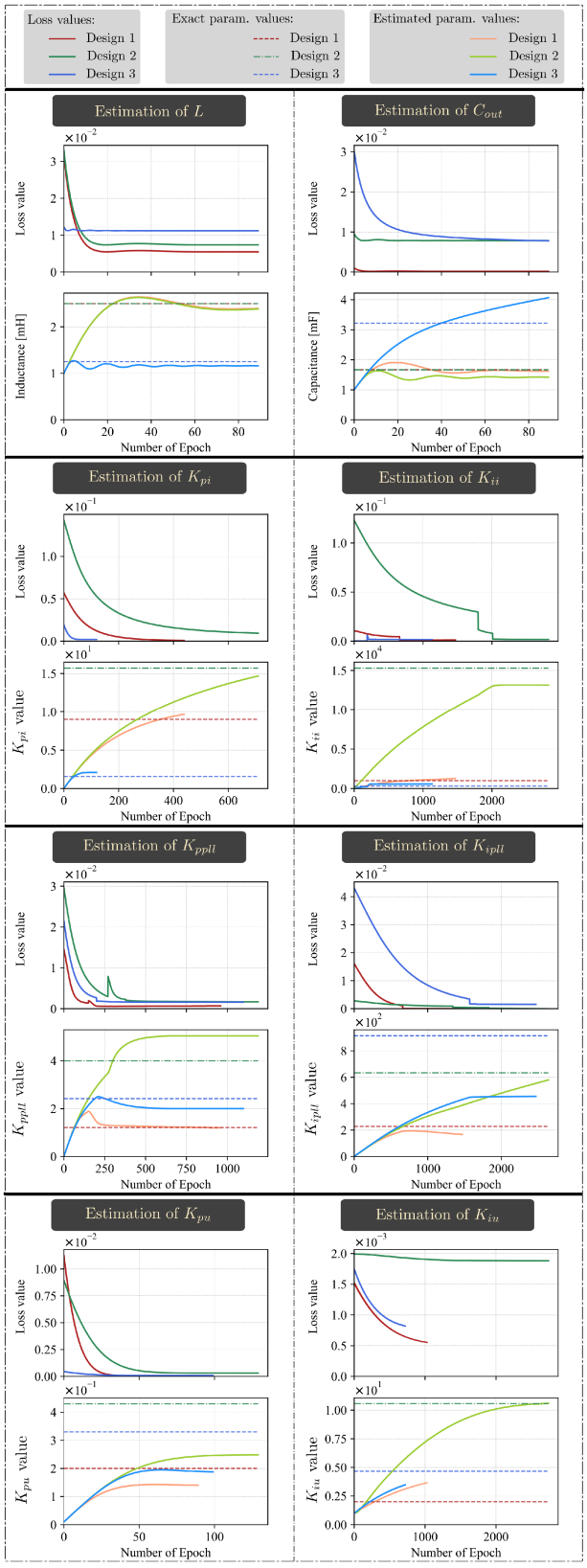

Fig. 10. Loss values during the optimization iteration and the estimated parameter values compared with the exact parameter values.

TABLE V
ESTIMATION RESULTS COMPARISON BETWEEN THE PROPOSED APPROACH AND THE NORMAL GD OPTIMIZATION APPROACH

Design 1			
	Exact	Proposed approach (error %)	Normal approach (error %)
L [mH]	2.5	2.4 (4%)	12.6 (404%)
K_{pi}	9	9.7 (8%)	0.39 (96%)
K_{ppll}	1.21	1.2 (1%)	0.43 (64%)
K_{ii}	1000	1264 (26%)	0.62 (100%)
K_{ipll}	228	166 (27%)	0.74 (100%)
C_{out} [mF]	1.67	1.62 (3%)	0.2 (88%)
K_{pu}	0.2	0.14 (30%)	0.37 (85%)
K_{iu}	2	3.63 (82%)	1.53 (24%)
Estimation time	N.A.	8 min	24 min
Design 2			
	Exact	Proposed approach (error %)	Normal approach (error %)
L [mH]	2.5	2.39 (4%)	12.9 (416%)
K_{pi}	15.7	14.69 (6%)	0.81 (95%)
K_{ppll}	4	5.04 (26%)	0.83 (79%)
K_{ii}	15297	13144 (14%)	1.86 (100%)
K_{ipll}	634	579 (9%)	1.7 (100%)
C_{out} [mF]	1.67	1.42 (15%)	0 (100%)
K_{pu}	0.43	0.25 (42%)	0.4 (7%)
K_{iu}	10.47	10.58 (1%)	2.34 (78%)
Estimation time	N.A.	17 min	46 min
Design 3			
	Exact	Proposed approach (error %)	Normal approach (error %)
L [mH]	1.25	1.16 (7%)	8.06 (545%)
K_{pi}	1.57	2.1 (34%)	0.47 (70%)
K_{ppll}	2.42	2.02 (17%)	0.44 (82%)
K_{ii}	306	558 (82%)	0.6 (100%)
K_{ipll}	914	453 (50%)	1.37 (100%)
C_{out} [mF]	3.21	4.08 (27%)	0.4 (88%)
K_{pu}	0.33	0.19 (42%)	0.61 (85%)
K_{iu}	4.66	3.45 (26%)	1.59 (66%)
Estimation time	N.A.	11 min	30 min

Fig. 12 illustrates the accuracy of the impedance estimated with the proposed approach at different operating points. As seen, at three different operating points, the estimated impedance is compared with the measured impedance and the exact impedance. Note that the exact impedance is obtained analytically by using the exact parameter values because the analytical model is verified in Section V-B. Fig. 12 shows that the estimated impedance matches the exact one at all operating points rather than only at $P = Q = 0$. Thus, it is verified that despite some errors in the identified parameter values, the estimated impedance has high accuracy. Furthermore, compared with the measured impedance, the estimated impedance shows similar accuracy for Z_{dd} and Z_{qq}. Nonetheless, for the coupling impedance, the estimated impedance is more accurate than the measured impedance when $|Z_{dq}|$ and $|Z_{qd}|$ are too small.

VI. CONCLUSION

This article proposes a GD optimization-based gray-box approach to obtain the HPEVC's input impedance. The simplified expression of the impedance elements $Z_{dd,dq,qd,qq}$ at the no-load condition is derived, which analytically reveals how the

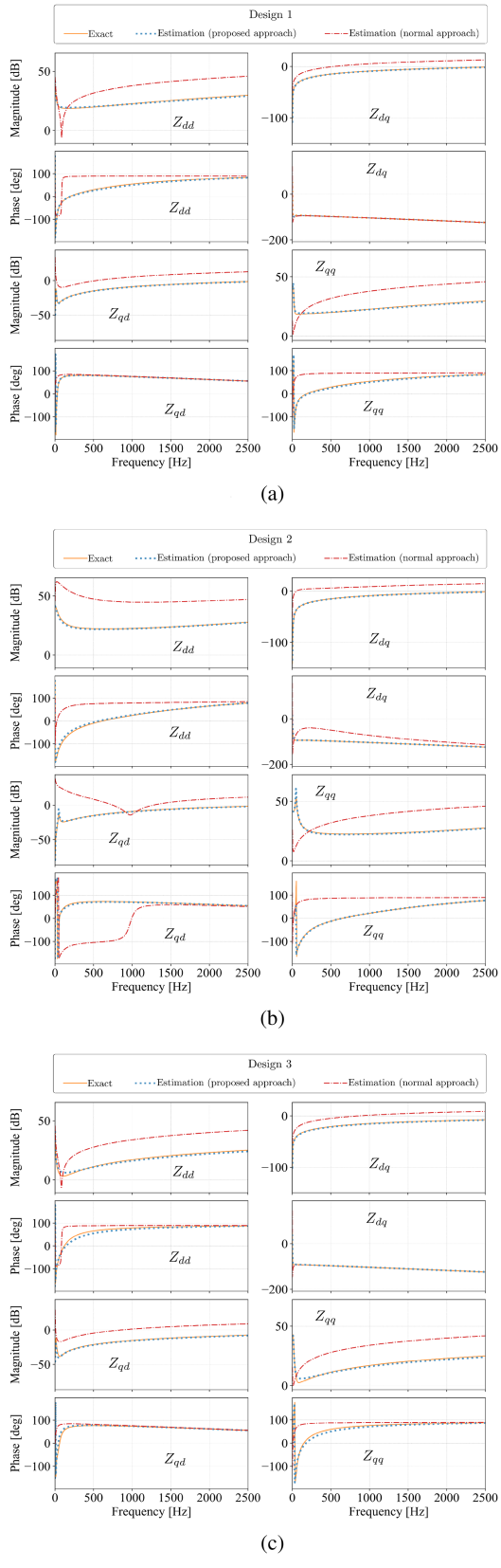

Fig. 11. Estimated impedance via the proposed approach compared with the exact impedance and the impedance estimated with the normal GD optimization-based approach when $P = Q = 0$ for the three designs. (a) Design 1. (b) Design 2. (c) Design 3.

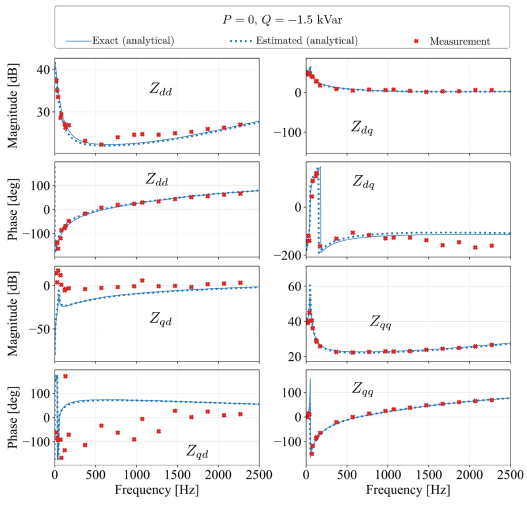

(a)

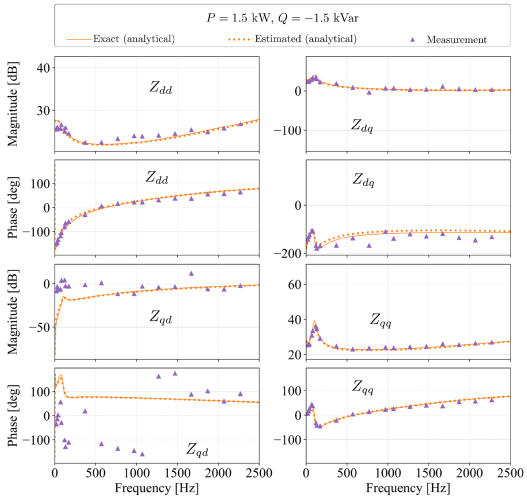

(b)

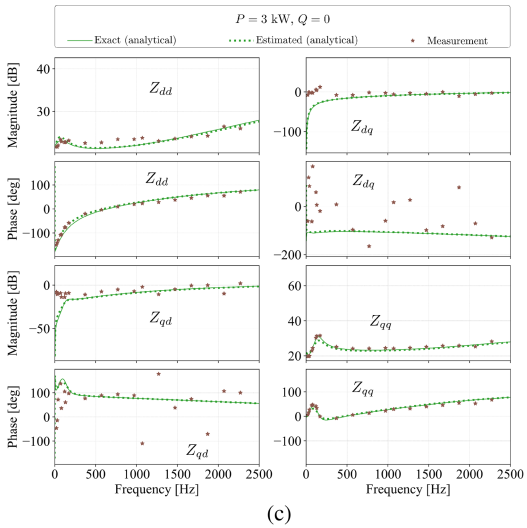

(c)

Fig. 12. At three different operating points, the measured impedance of the AFE (Design 2) is compared with the exact impedance (analytical) and the estimated impedance (analytical). (a) $P = 0$ and $Q = -1.5$ kVar. (b) $P = 1.5$ kW and $Q = -1.5$ kVar. (c) $P = 3$ kW and $Q = 0$.

controller and circuit parameters shape the impedance. Furthermore, the influential frequency ranges of the eight parameters to be identified are analyzed. Based on the revealed influential frequency range of the parameters, a GD optimization-based estimation algorithm is proposed to identify the parameters in sequence. Only the sensitive impedance segment for each parameter is selected for the estimation. As a result, the proposed estimation algorithm can achieve higher estimation accuracy and less time cost compared to a conventional counterpart, which is validated by experiment tests. Finally, the proposed gray-box modeling approach is validated with experimental tests. Compared to the measured impedance, the impedance extracted with the proposed approach has a higher accuracy for the coupling elements, namely, Z_{dq} and Z_{qd}, especially when the PF is higher, and a comparable accuracy for the diagonal elements, namely, Z_{dd} and Z_{qq}. Moreover, the performance of the approach is evaluated with three designs with different controller and circuit parameters, evincing the effectiveness of the approach in different situations.

APPENDIX

$$\boldsymbol{G_i}(s) = \begin{bmatrix} K_{pi} + \frac{K_{ii}}{s} & 0 \\ 0 & K_{pi} + \frac{K_{ii}}{s} \end{bmatrix}, \boldsymbol{G_v}(s) = \begin{bmatrix} K_{\text{pu}} + \frac{K_{iu}}{s} \\ 0 \end{bmatrix}$$

$$\boldsymbol{G}_{\text{del}}(s) = \begin{bmatrix} e^{-sT_{\text{del}}} & 0 \\ 0 & e^{-sT_{\text{del}}} \end{bmatrix}, \boldsymbol{Y}(s) = \begin{bmatrix} Ls + R & 0 \\ 0 & Ls + R \end{bmatrix}$$

$$\boldsymbol{I} = \begin{bmatrix} 1 & 0 \\ 0 & 1 \end{bmatrix}, \boldsymbol{J} = \begin{bmatrix} 0 & -1 \\ 1 & 0 \end{bmatrix}$$

$$\boldsymbol{T}_{\text{pll}}(s) = \begin{bmatrix} 0 & \frac{K_{p\text{pll}}s + K_{i\text{pll}}}{(K_{p\text{pll}}s + K_{i\text{pll}})E_d + s^2} \end{bmatrix}$$

$$K(s) = \frac{3}{2(C_{\text{out}}s + 1/Z_{\text{dc}}(s))}.$$

REFERENCES

[1] L. Wang, Z. Qin, T. Slangen, P. Bauer, and T. van Wijk, "Grid impact of electric vehicle fast charging stations: Trends, standards, issues and mitigation measures—An overview," *IEEE Open J. Power Electron.*, vol. 2, pp. 56–74, Jan. 26, 2021.

[2] B. Basta and W. Morsi, "Low and high order harmonic distortion in the presence of fast charging stations," *Int. J. Elect. Power Energy Syst.*, vol. 126, 2021, Art. no. 106557.

[3] Z. Qin, L. Wang, and P. Bauer, "Review on power quality issues in EV charging," in *Proc. IEEE 20th Int. Power Electron. Motion Control Conf.*, 2022, pp. 360–366.

[4] J. Enslin and P. Heskes, "Harmonic interaction between a large number of distributed power inverters and the distribution network," *IEEE Trans. Power Electron.*, vol. 19, no. 6, pp. 1586–1593, Nov. 2004.

[5] C. Buchhagen, C. Rauscher, A. Menze, and J. Jung, "Borwin1—First experiences with harmonic interactions in converter dominated grids," in *Proc. Int. ETG Congr.; Die Energiewende—Blueprints New Energy Age*, 2015, pp. 1–7.

[6] J. Sun, "Impedance-based stability criterion for grid-connected inverters," *IEEE Trans. Power Electron.*, vol. 26, no. 11, pp. 3075–3078, Nov. 2011.

[7] L. B. Larumbe, Z. Qin, and P. Bauer, "Guidelines for stability analysis of the DDSRF-PLL using LTI and LTP modelling in the presence of imbalance," *IEEE Open J. Ind. Electron. Soc.*, vol. 3, pp. 339–352, May 2022, doi: 10.1109/OJIES.2022.3178042.
[8] J. Lei, Z. Qin, W. Li, P. Bauer, and X. He, "Stability region exploring of shunt active power filters based on output admittance modeling," *IEEE Trans. Ind. Electron.*, vol. 68, no. 12, pp. 11696–11706, Dec. 2021.
[9] L. Wang, Z. Qin, L. B. Larumbe, and P. Bauer, "Python supervised co-simulation for a day-long harmonic evaluation of EV charging," *Chin. J. Elect. Eng.*, vol. 7, no. 4, pp. 15–24, 2021.
[10] B. Wen, D. Boroyevich, R. Burgos, P. Mattavelli, and Z. Shen, "Analy+f D-Q small-signal impedance of grid-tied inverters," *IEEE Trans. Power Electron.*, vol. 31, no. 1, pp. 675–687, Jan. 2016.
[11] X. Wang, L. Harnefors, and F. Blaabjerg, "Unified impedance model of grid-connected voltage-source converters," *IEEE Trans. Power Electron.*, vol. 33, no. 2, pp. 1775–1787, Feb. 2018.
[12] L. B. Larumbe, Z. Qin, L. Wang, and P. Bauer, "Impedance modeling for three-phase inverters with double synchronous reference frame current controller in the presence of imbalance," *IEEE Trans. Power Electron.*, vol. 37, no. 2, pp. 1461–1475, Feb. 2022.
[13] J. Sun, "Input impedance analysis of single-phase PFC converters," *IEEE Trans. Power Electron.*, vol. 20, no. 2, pp. 308–314, Mar. 2005.
[14] B. Sohlberg and E. W. Jacobsen, "Grey box modelling—branches and experiences," *IFAC Proc. Volumes*, vol. 41, no. 2, pp. 11415–11420, 2008.
[15] J. Y. Hung, "Parameter estimation using sensitivity points: Tutorial and experiment," *IEEE Trans Ind. Electron.*, vol. 48, no. 6, pp. 1043–1047, Dec. 2001.
[16] R. S. Blom and P. M. J. Van den Hof, "Multivariable frequency domain identification using IV-based linear regression," in *Proc. 49th IEEE Conf. Decis. Control*, 2010, pp. 1148–1153.
[17] C. C. Brozio and H. J. Vermeulen, "Wideband equivalent circuit modelling and parameter estimation methodology for two-winding transformers," *IEE Proc. Gener., Transmiss. Distrib*, vol. 150, no. 4, pp. 487–492, 2003.
[18] S. D. Mitchell and J. S. Welsh, "Initial parameter estimates and constraints to support gray box modeling of power transformers," *IEEE Trans. Power Del.*, vol. 28, no. 4, pp. 2411–2418, Oct. 2013.
[19] B. Long, Z. Zhu, W. Yang, K. T. Chong, J. Rodríguez, and J. M. Guerrero, "Gradient descent optimization based parameter identification for FCS-MPC control of LCL-type grid connected converter," *IEEE Trans. Ind. Electron.*, vol. 69, no. 3, pp. 2631–2643, Mar. 2022.
[20] M. Amin and M. Molinas, "A gray-box method for stability and controller parameter estimation in HVDC-connected wind farms based on nonparametric impedance," *IEEE Trans. Ind. Electron.*, vol. 66, no. 3, pp. 1872–1882, Mar. 2019.
[21] R. Ge, F. Huang, C. Jin, and Y. Yuan, "Escaping from saddle points-online stochastic gradient for tensor decomposition," in *Proc. Conf. Learn. Theory*, 2015, pp. 797–842.
[22] A. Ahmad, Z. Qin, T. Wijekoon, and P. Bauer, "An overview on medium voltage grid integration of ultra-fast charging stations: Current status and future trends," *IEEE Open J. Ind. Electron. Soc.*, vol. 3, pp. 420–447, Jun. 2022, doi: 10.1109/OJIES.2022.3179743.
[23] L. Harnefors, "Modeling of three-phase dynamic systems using complex transfer functions and transfer matrices," *IEEE Trans. Ind. Electron.*, vol. 54, no. 4, pp. 2239–2248, Aug. 2007.
[24] M. P. Kazmierkowski, R. Krishnan, and F. Blaabjerg, *Control in Power Electronics*, vol. 17. Amsterdam, The Netherlands:Elsevier, 2002.
[25] S. Golestan and J. M. Guerrero, "Conventional synchronous reference frame phase-locked loop is an adaptive complex filter," *IEEE Trans. Ind. Electron.*, vol. 62, no. 3, pp. 1679–1682, Mar. 2015.
[26] M. Liserre, F. Blaabjerg, and A. Dell'Aquila, "Step-by-step design procedure for a grid-connected three-phase PWM voltage source converter," *Int. J. Electron.*, vol. 91, no. 8, pp. 445–460, 2004.
[27] L. Harnefors, M. Bongiorno, and S. Lundberg, "Input-admittance calculation and shaping for controlled voltage-source converters," *IEEE Trans. Ind. Electron.*, vol. 54, no. 6, pp. 3323–3334, Dec. 2007.
[28] J. Dannehl, C. Wessels, and F. W. Fuchs, "Limitations of voltage-oriented PI current control of grid-connected PWM rectifiers with LCL filters," *IEEE Trans. Ind. Electron.*, vol. 56, no. 2, pp. 380–388, Feb. 2009.
[29] K. Li, A. Formentini, D. Dewar, and P. Zanchetta, "Controller design of an active front-end converter keeping in consideration grid dynamic interaction," *IEEE Trans. Ind. Electron.*, vol. 69, no. 5, pp. 5195–5206, May 2022.
[30] D. Dong, B. Wen, D. Boroyevich, P. Mattavelli, and Y. Xue, "Analysis of phase-locked loop low-frequency stability in three-phase grid-connected power converters considering impedance interactions," *IEEE Trans. Ind. Electron.*, vol. 62, no. 1, pp. 310–321, Jan. 2015.
[31] Y. N. Dauphin, R. Pascanu, C. Gulcehre, K. Cho, S. Ganguli, and Y. Bengio, "Identifying and attacking the saddle point problem in high-dimensional non-convex optimization," in *Proc. 27th Int, Conf. Adv. Neural Inf. Process. Syst.*, vol. 27, 2014, pp. 2933–2941.
[32] D. P. Kingma and J. Ba, "ADAM: A method for stochastic optimization," 2014, *arXiv:1412.6980*.

Lu Wang (Student Member, IEEE) received the B.Sc. degree in electrical engineering from the Beijing Institute of Technology, Beijing, China, in 2015 and the M.Sc. degree (*cum laude*) in electrical sustainable engineering in 2018 from the Delft University of Technology, Delft, The Netherlands, where he is currently working toward the Ph.D. degree in power quality of EV charging with the DC Systems, Energy Conversion and Storage Group (DCE&S).

His research interests include power quality and stability issues induced by EV charging.

Zian Qin (Senior Member, IEEE) received the B.Eng. degree from Beihang University, Beijing, China, in 2009, the M.Eng. degree from the Beijing Institute of Technology, Beijing, China, in 2012, and the Ph.D. degree from Aalborg University, Aalborg, Denmark, in 2015, all in electrical engineering.

He is currently an Assistant Professor with Delft University of Technology, Delft, The Netherlands. In 2014, he was a Visiting Scientist with Aachen University, Aachen, Germany. He has authored/coauthored more than 100 journals/conference papers, four book chapters, two international patents, and also worked on several European and Dutch national projects in these areas. His research interests include power quality and stability of power electronics-based grid, and solid-state transformers.

Dr. Qin is currently an Associate Editor for the IEEE TRANS INDUSTRIAL ELECTRONICS, and a Guest Associate Editor for the IEEE JOURNAL OF EMERGING AND SELECTED TOPICS and IEEE TRANS ENERGY CONVERSION. He is a Distinguished Reviewer for 2020 of IEEE TRANSACTIONS OF INDUSTRIAL ELECTRONICS. He was the Technical Program Chair of IEEE International Symposium on Power Electronics for Distributed Generation Systems 2023, IEEE International Symposium on Industrial Electronics 2020, IEEE Workshop on Control and Modeling for Power Electronics 2020, etc.

Pavol Bauer (Senior Member, IEEE) received the master's degree in electrical engineering from the Technical University of Kosice, Kosice, Slovakia, in 1985 and the Ph.D. degree in power electronics from the Delft University of Technology, Delft, The Netherlands, in 1995.

From 2002 to 2003, he was with KEMA (DNV GL), Arnhem, The Netherlands. He is currently a Full Professor with the Department of Electrical Sustainable Energy, Delft University of Technology, and the Head of DC Systems, Energy Conversion, and Storage Group. He is also a Professor with the Brno University of Technology, Brno, Czech Republic, and an Honorary Professor with the Politehnica University Timisoara, Timisoara, Romania. He has authored/coauthored eight books and more than 120 journal articles and 500 conference papers. He holds seven international patents and organized several tutorials at international conferences. He has worked on many projects for the industry concerning wind and wave energy, power electronic applications for power systems, such as Smarttrafo; HVdc systems, projects for smart cities such as photovoltaic (PV) charging of electric vehicles, PV and storage integration, contactless charging; and he participated in several Leonardo da Vinci and H2020, and Electric Mobility Europe EU projects as a Project Partner (ELINA, INETELE, E-Pragmatic, Micact, Trolley 2.0, OSCD, P2P, and Progressus) and a Coordinator (PEMCWebLab.com-Edipe, SustEner, Eranet DCMICRO).

Dr. Bauer is the Former Chairman of Benelux IEEE Joint Industry Applications Society, Power Electronics and Power Engineering Society Chapter, the Chairman of the Power Electronics and Motion Control Council, a Member of the Executive Committee of European Power Electronics Association, and also a Member of the International Steering Committee at numerous conferences.